

# Theoretical analysis of injection driven thermal light emitters based on graphene encapsulated by hexagonal boron nitride

V Ryzhii<sup>1,2</sup>, T Otsuji<sup>1</sup>, M Ryzhii<sup>3</sup>, V Leiman<sup>4</sup>, P P Maltsev<sup>2</sup>,  
V E Karasik<sup>5</sup>, V Mitin<sup>6</sup>, and M S Shur<sup>7</sup>

<sup>1</sup>Research Institute of Electrical Communication, Tohoku University,  
Sendai 980-8577, Japan

<sup>2</sup>Mokerov Institute of Ultra High Frequency Semiconductor Electronics, RAS,  
Moscow 117105, Russia

<sup>3</sup>Department of Computer Science and Engineering, University of Aizu,  
Aizu-Wakamatsu 965-8580, Japan

<sup>4</sup>Center for Photonics and Two-Dimensional Materials, Moscow Institute of Physics  
and Technology, Dolgoprudny 141700, Russia

<sup>5</sup>Center of Photonics and Infrared Engineering, Bauman Moscow State Technical  
University, Moscow 111005, Russia

<sup>6</sup>Department of Electrical Engineering, University at Buffalo SUNY,  
Buffalo, NY 14260-1920, USA

<sup>7</sup>Departments of Electrical, Computer, and Systems Engineering and Physics,  
Applied Physics, and Astronomy, Rensselaer Polytechnic Institute,  
Troy, NY 12180, USA

E-mail: v-ryzhii@riec.tohoku.ac.jp

**Abstract.** We develop the device model for the proposed injection (electrically) driven thermal light emitters (IDLEs) based on the vertical Hexagonal Boron Nitride Layer/Graphene Layer/ Hexagonal Boron Nitride Layer (hBNL/GL/hBNL) heterostructures and analyze their dynamic response. The operation of the IDLEs is associated with the light emission of the hot two-dimensional electron-hole plasma (2DEHP) generated in the GL by both the lateral injection from the side contacts and the vertical injection through the hBNL (combined injection) heating the 2DEHP. The temporal variation of the injection current results in the variation of the carrier effective temperature and their density in the GL leading to the modulation of the output light. We determine the mechanisms limiting the IDLE efficiency and the maximum light modulation frequency. A large difference between the carrier and lattice temperatures the IDLEs with an effective heat removal enables a fairly large modulation depth at the modulation frequencies about dozen of GHz in contrast to the standard incandescent lamps. We compare the IDLEs with the combined injection under consideration and IDLEs using the carrier Joule heating by lateral current. The obtained results can be used for the IDLE optimization.

*Keywords:* graphene, hexagonal boron nitride, light emitter, carrier heating, injection, dynamic response

## 1. Introduction

Heterostructures with graphene layers (GLs) are promising building blocks for infrared and terahertz photodetectors [1–14], optical modulators [15–18], plasmonic and frequency multiplication devices [19–28], and lasers and light-emitting diodes [29–44] (including those based on hybrid GL/black phosphorous devices [45, 46]). The realization of the on-chip monolithic nanoscale relatively simple light sources for high-bandwidth inter- and intra-chip connections is still a challenging problem [47]. There are several proposals and realizations of the compact and simple GL thermal light sources using the electrical carrier heating in the GLs [48–55]. Such GL-base thermal light sources can be fairly effective and very fast [54]. The operation and, in particular, the operation speed of the GL-based thermal sources are determined by complex relaxation and recombination mechanisms, namely, of the carrier-carrier scattering, the interaction of the hot carriers in the GL with the GL optical phonons and the interface optical phonons and the optical phonons in the media surrounding the GL. The carrier heating in the GLs in the devices in question can be associated with the Joule heating by the electric current flowing in the GL between the side contacts to the GL [48–55]. Another option is to use the combined carrier injection (the injection of relatively cold carriers from the side contact(s) and the vertical injection of the not too hot carriers from the top contact). This concept was recently applied to the GL heterostructures [44–46] aiming to realize the interband population inversion in the GLs for its use for far-infrared and terahertz lasing or superluminescence (the combined carrier injection is widely

used in the standard vertical-cavity surface emitting heterostructure lasers). In such heterostructure devices the vertical injection should not lead to a marked heating of the two-dimensional electron-hole plasma (2DEHP) in the GL. This is why the black phosphorus (BP) (or similar materials) having relatively small band off-sets at the heterointerface [56, 57] were chosen for the emitter contact layer. In contrast, the thermal electrically driven light sources (IDLEs) require strong heating of the 2DEHP in the GLs. The thermal IDLEs, in particularly those based on the GLs encapsulated by the hBNs, exhibit the following features. First of all, both the optical phonon and acoustic phonon systems can be relatively hot (their effective temperatures substantially exceed the temperature of the thermostat) when the carriers are hot. Second, the Auger recombination-generation processes [58] can be much more effective than those at moderate or low carrier temperatures.

This is why, the use of the emitter contact layer made of the black phosphorus (BP) (or similar materials) having relatively small band off-sets at the GL/black phosphorus [56, 57] interface was proposed. However, in contrast, in the injection driven thermal light sources (IDLEs) a strong heating of the 2DEHP in the GLs is desirable. These thermal light sources, in particular those based on the GLs encapsulated by the IDLEs, exhibit the following features. First of all, at sufficiently hot carrier, both the optical phonon and acoustic phonon systems can also be relatively hot (their effective temperatures substantially exceed the temperature of the thermostat). Second, the Auger recombination-generation processes [58] can be much more effective than at moderate or low carrier temperatures.

In this paper, we study the thermal IDLEs based on the GL/hBN heterostructures with

the combined lateral/vertical carrier injection providing an effective heating due to rather large the GL/hBN band off-sets. We focus on the dynamic properties of these sources, which can be used in different opto-electron systems. In particular, we compare the characteristics of the IDLE in question with the similar IDLE using the vertical double injection and the Joule heating and demonstrate that the IDLEs with the combined and double vertical injection can be faster due to a higher sensitivity to the variations of the controlling voltage.

The paper is organized as follows. In Section 2, we present the proposed IDLE device structure and formulate the pertinent mathematical model. In Section 3, we use this model for the calculations of the steady-state effective temperatures of the carrier, optical phonon, and lattice (acoustic phonon) systems as functions of the injected carrier current and the structural parameters. Apart from the numerical solution of the equations of the model, we analytically analyze their asymptotic behavior in the limiting cases. Section 4 deals with the calculations of the spectrum of the light emitted by the IDLEs and the output power at the steady-state carrier injection. For this, we use the data for the effective temperatures obtained in Section 3. In Section 5, we analyze the modulation of the output light by the ac injection current characteristics and evaluate the IDLE maximum modulation frequency. Section 6 is devoted to the derivation of the light modulation depth as a function of the modulation ac voltage. In Sections 7 and 8, we comment the obtained results and formulate the conclusions. Some mathematical details are singled out to the Appendix.

## 2. Device structures and mathematical model

Figure 1 shows the schematic views of the IDLEs based on the hBNL/GL/hBNL heterostructures with the combined (vertical-lateral) and double vertical injection. The GLs in the IDLE with the combined injection are supplied by the side contacts providing the electron injection to the GLs. The heterostructure top comprises an undoped or lightly doped hBN layer and a cap, which is heavily doped by acceptors. Such a  $p^+$ - $p$ -hBNL region serves as an injector of holes into the GL. Here we focus on the IDLE with the vertical hole injection and the lateral electron injection [see figures 1(a) and 1(c)]. The obtained results can be easily extended for the IDLEs with the combined injection can be based on the heterostructures  $n^+$ - $n$ -hBN vertical injector and the lateral hole injection and the IDLEs with the vertical double injection (see below). The IDLEs under consideration can comprise the multiple- and single GLs. The device structure can be placed on a  $\text{SiO}_2$  substrate.

Our mathematical model (which is the generalized version of those used previously [44–46], see also more early works [31, 59]) corresponds to the following scenario:

- (i) The injected hot holes transfer their energy partially to different optical phonon modes (intra-valley and inter-valley phonons in the GL and the interface phonons. (emitting the cascades of these phonons) and partially to the 2DEHP via the injected hole collisions with the 2DEHP electrons and holes;
- (ii) The 2DEHP heated by the injected holes transfer the excessive energy to the optical phonon systems [60];
- (iii) The optical phonon system transfers the energy to the acoustic phonons (lattice) due to

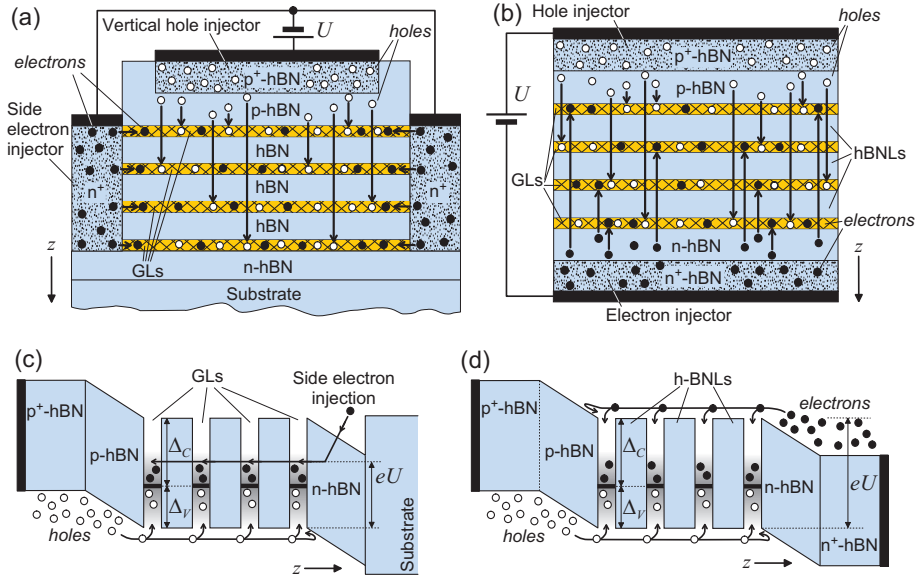


**Figure 1.** Schematic views of the IDLE based on heterostructures (a) with the top  $p^+$ - $p$ -hBN vertical hole injector and the GLs separated by the hBNs and supplied with the  $n^+$  side contacts and (b) with the top  $p^+$ - $p$ -hBN hole and bottom  $n^+$ - $n$ -hBN vertical injectors and the band diagrams of (c) the IDLE with vertical-lateral injection and (d) vertical double injection under applied voltage  $U$ . Opaque and open circles correspond to electrons and holes, respectively. Arrows show the carrier movement directions

the anharmonic optical and interface phonons decay [61–65];

(iv) The hot acoustic phonons bring their thermal energy primarily [55] to the top or bottom contact serving as the heat sink;

(v) The deviation of the electron and hole densities from the equilibrium ones is controlled by the interband recombination-generation processes involving the optical phonons [31, 59, 60] and the Auger processes [58, 66].

It is assumed that the carrier-carrier interactions in the 2DEHP are sufficiently strong, so that both the electron and hole components have the common effective temperature  $T$ , which is generally different from the effective optical phonon temperature  $\Theta$ , the acoustic phonon temperature  $T_L$  [the lattice temperature around the GL(s)], and the sink (vertical contact, thermostat) temperature  $T_C$ . Due to the latter, the electron and hole energy distribution functions are  $f_e(\varepsilon_e) = \{1 +$

$\exp[(\varepsilon_e - \mu_e)]/T\}^{-1}$  and  $f_h(\varepsilon_h) = \{1 + \exp[(\varepsilon_h - \mu_h)]/T\}^{-1}$  with  $\varepsilon_e$ ,  $\varepsilon_h$ ,  $\mu_e$ , and  $\mu_h$  being the pertinent kinetic carrier energies and quasi-Fermi energies counted from the GL Dirac point. This assumption is particularly reasonable for the IDLEs due to their operation at elevated carrier densities. For simplicity, we do not distinguish different optical modes assuming that the optical phonon system is characterized by a single effective phonon energy  $\hbar\omega_O$ , which accounts for the intra-valley (with the energy  $\sim 200$  meV), inter-valley ( $\sim 165$  meV), and interface ( $\sim 100$  meV) optical phonons.

Considering the abovementioned processes, namely the intraband and interband emission and absorption of optical phonons [62], the decay of these phonons into the acoustic phonons, and the Auger recombination-generation processes as the main mechanisms determining the carrier den-

sity and energy balances in the 2DEHP, the main equations of the model can be presented in the following form:

$$\frac{d\Sigma}{dt} = \frac{j}{e} - R_0^{inter} - R_A, \quad (1)$$

$$\frac{d\mathcal{E}}{dt} = \frac{j}{e}\overline{\Delta}_i - \hbar\omega_0(R_0^{inter} + R_0^{intra}). \quad (2)$$

Here  $\Sigma$  and  $\mathcal{E}$  are the 2DEHP density (the net density of the electrons and holes in the GL) and their energy, respectively,  $j$  is the density of the vertically injected current into a GL (in the cases of the IDLEs with a single GL and multiple GLs,  $j = j_i$  and  $j = j_i/n$ , respectively, where  $j_i$  is the density of the net injected current and  $n$  is the number of the GLs [44]),  $\overline{\Delta}_i$  is the energy transferred by one vertically injected holes directly to the 2DEHP (taking into account that a fraction of the injected hole energy  $\Delta_i$  goes to the optical phonons), and  $e = |e|$  is the electron charge. The terms  $R_0^{inter}$ ,  $R_0^{intra}$ , and  $R_A$  are the rates of the interband and intraband transitions associated with the pertinent optical phonons and the Auger recombination-generation processes; their explicit forms are presented in the Appendix. The average energy brought to the 2DEHP by an injected hole is estimated as [58]

$$\overline{\Delta}_i = \Delta_i - k_0\hbar\omega_0. \quad (3)$$

Here  $\Delta_i = \Delta_V + 3T_0/2$ ,  $T_0$  is the hole temperature in the  $p^+$  injector, coinciding with the metal contact temperature (which serves as the heat sink). Equation (3) shows that each injected hole energy (with the average injected kinetic energy  $\varepsilon_i = \Delta_V + 3T_0/2$ ) transferred directly to the 2DEHP is smaller than  $\varepsilon_i$  because a portion,  $k_0\hbar\omega_0$ , of this energy

goes immediately to the optical phonons. If we disregard the energy dependence of the time,  $\tau_0$ , of the optical phonon emission, the average numbers of the optical phonons of the given sort generated by the injected hole is equal to  $k_0 = \frac{1}{\tau_0/\tau_{cc}} \left[ 1 - \frac{1}{(1 + \tau_0/\tau_{cc})^{K_0}} \right]$ , where  $K_0$  is the maximum numbers of the optical phonons in the cascade emitted by the hole after its injection (see the Appendix). Since the density of states in GLs virtually linearly increases with the carrier energy, one might assume that the optical phonon intraband emission decreases with the energy. In this case,  $k_0 = K_0/(1 + \tau_0/\tau_{cc})$ . Setting  $\Delta_V = 1200$  meV,  $T_0 = 25$  meV,  $K_0 = 8$ , one obtains  $\Delta_i \simeq 1240$  meV and  $\overline{\Delta}_i \simeq 1090 - 1210$  meV (i.e., for the above two cases,  $\Delta_i \lesssim \Delta_V$ ).

Considering the deviation optical phonons distribution function  $\mathcal{N}_0 = [\exp(\hbar\omega_0/\Theta) - 1]^{-1}$  from the distribution function of optical phonons,  $\mathcal{N}_0^{eq} = [\exp(\hbar\omega_0/T_L) - 1]^{-1}$ , in equilibrium with the acoustic phonons in the vicinity of the GL (where  $T_L$  is the lattice temperature or the effective temperature of acoustic phonons in the vicinity of the GL), for  $\mathcal{N}_0$  we obtain

$$\frac{d\mathcal{N}_0}{dt} = \frac{T_L}{T_0} \frac{(\mathcal{N}_0^{eq} - \mathcal{N}_0)}{\tau_D} + \frac{1}{\overline{\Sigma}_0} \left( R_0^{inter} + R_0^{intra} + \frac{jk_0}{e} \right). \quad (4)$$

Here  $\overline{\Sigma}_0 = (1/2\pi)(\hbar\omega_0/\hbar v_W)^2$  is the characteristic carrier density determined by the energy dependence of the density of state in the GL (see the Appendix),  $\hbar$  is the Planck constant, and  $v_W \simeq 10^8$  cm/s is the electron and hole velocity in GLs. The quantity  $\overline{\Sigma}_0/\tau_0$  is estimated using the data on the carrier interband generation-recombination rate [59] and  $\tau_D$  is the time of the optical phonon decay due to the unharmonic lattice processes at

$T_L = T_0$ . Theoretical and experimental studies for  $\tau_D$  in GLs at room lattice temperature [60–63] yield the values in the range from 1 to 5 ps. However, this time can be much shorter:  $\tau_D \simeq 0.20 - 0.35$  ps in the GLs encapsulated by the hBNs due to the role of the interface optical phonons. The factor  $T_L/T_0$  reflects an increase in the optical phonon decay rate (an increase in the decay time) with rising lattice temperature (the effective temperature of acoustic phonons) [67]. This temperature dependence arises from the dependence of the unharmonic decay process on the "daughter" acoustic phonon modes population [67, 68]. The lattice temperature  $T_L$  is determined by the power injected into the GL and by the thermal conductivity the per unit area,  $C$ , of the layers surrounding the GL, i.e., the hBNs and the metal contact. Neglecting the lateral heat transfer to the side contacts [48–50], the lattice temperature,  $T_L$ , around the GL can be determined from the following equation:

$$C\tau_L \frac{dT_L}{dt} = C(T_0 - T_L) + \frac{j\Delta_i}{e}. \quad (5)$$

Here  $\tau_L$  is the characteristic time of the lattice heating and cooling down that is proportional to the lattice heat capacitance  $c_L$ .

The efficiency of the 2DEHP, optical phonon systems, and the lattice temperature crucially depends on the thermal conductivity  $C$ , i.e., on the the hBNs thermal conductance of  $c$  ( $C \propto c$ ). If the metal contact really serves as the heat sink, i.e., if the contact temperature is close to room temperature, considering the hBNs thermal conductance of  $c \simeq 20\text{W/m}\cdot\text{K}$  [69], for the hBNs of the thickness  $L_{hBN} = (1 - 2) \mu\text{m}$ , we obtain  $C = c/L_{hBN} \simeq (1 - 2) \text{kW/cm}^2\text{K}$ . However, when the cooling down of the top metal contact is limited by the heat transfer to the surrounding air, the quantity  $C$  can be several orders of magnitude smaller.

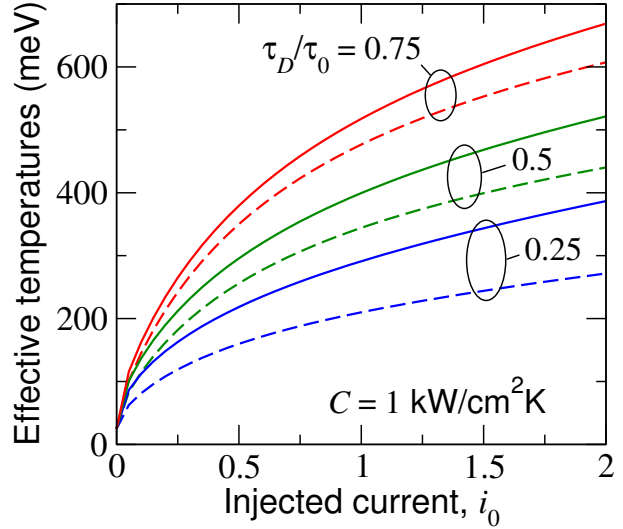


**Figure 2.** Effective carrier temperature  $T$  (solid lines) and optical phonon temperature  $\Theta$  (dashed lines) versus the normalized injected current  $i_0$  for  $\Delta_i = 1240$  meV,  $\overline{\Delta}_i = 1210$  meV,  $C = 1 \text{ kW/cm}^2\text{K}$ ,  $T_0 = 25$  meV, and different values of the optical phonon decay time  $\tau_D/\tau_0 = 0.25 - 0.75$  ps.

### 3. Steady-state effective temperatures

#### 3.1. Numerical analysis

Consider first the case of the dc injection current  $j = j_0 = \text{const}$ . At  $j_0 = 0$ , equations (4) - (6) naturally yield  $\mathcal{N}_0 = \mathcal{N}_0^{\text{eq}}$ , i.e.,  $\Theta = T_L = T_0$ , and  $\mu_e + \mu_h = 0$ . Using the steady-stater versions of equations (1) and (2) (see the Appendix), we obtain

$$\left[ (\mathcal{N}_0 + 1) \exp\left(\frac{\mu_e + \mu_h - \hbar\omega_0}{T}\right) - \mathcal{N}_0 \right] + \frac{\tau_0}{\tau_A} \left[ \exp\left(\frac{\mu_e + \mu_h}{T}\right) - 1 \right] = i_0, \quad (6)$$

$$\left[ (\mathcal{N}_0 + 1) \exp\left(\frac{\mu_e + \mu_h}{T}\right) \exp\left(-\frac{\hbar\omega_0}{T}\right) - \mathcal{N}_0 \right] + \frac{1}{\eta_0} \left[ (\mathcal{N}_0 + 1) \exp\left(-\frac{\hbar\omega_0}{T}\right) - \mathcal{N}_0 \right] = i_0 \frac{\overline{\Delta}_i}{\hbar\omega_0}. \quad (7)$$

Here  $i_0 = j_0/\bar{j}$ , where  $\bar{j} = e\overline{\Sigma}_0/\tau_0 = eG_0 \exp(\hbar\omega_0/T)$ ,  $\eta_0 \simeq (\hbar\omega_0/\pi T)^2$  [59].

The quantity  $\eta_0$  characterizes the relative contributions to the 2DEHP energy relaxation due to the interband and intraband transitions mediated by the optical phonons. In the case of rather hot carriers, the intraband processes involve wide energy ranges, so that  $\eta_0$  can be close to unity. The characteristic injection current density  $\bar{j}$ , determined by the parameters of carrier scattering on different optical phonon modes, can be treated as a main fitting parameter of the model under consideration. For definiteness, in the following assuming that the rate of the electron-hole pairs interband generation due to the absorption of the thermal optical phonons at  $T_0 = 25$  meV and the characteristic ("average") photon energy are equal to  $G_0 = 2 \times 10^{21}$  cm<sup>-2</sup>s<sup>-1</sup> and  $\hbar\omega_0 = 150$  meV, respectively (see the Appendix). We also set  $\bar{\Sigma}_0/\tau_0 = 2 \times 10^{24}$  cm<sup>-2</sup>s<sup>-1</sup>, so that  $\tau_0 \simeq 0.42$  ps and  $\bar{j} \simeq 320$  kA/cm<sup>2</sup>.

Due to a large ratio  $\Delta_i/\hbar\omega_0$  and a smallness of  $\tau_A/\tau_0$  in the situations under consideration, the right-hand side of equation (A6) can be simplified and we obtain, so that from equations (6) and (7)

$$\left(1 + \frac{1}{\eta_0}\right) \left[ (\mathcal{N}_0 + 1) \exp\left(-\frac{\hbar\omega_0}{T}\right) - \mathcal{N}_0 \right] \simeq i_0 \left( \frac{\bar{\Delta}_i}{\hbar\omega_0} \right). \quad (8)$$

Accounting for the explicit expression for the terms in its right-hand side (see the Appendix) equation (4) yields

$$\mathcal{N}_0 = \frac{1}{\exp(\hbar\omega_0/T_L) - 1} + i_0 \frac{\Delta_i}{\hbar\omega_0} \frac{\tau_D}{\tau_0} \frac{T_0}{T_L}, \quad (9)$$

or

$$\Theta = \frac{\hbar\omega_0}{\ln \left\{ 1 + \frac{\exp\left(\frac{\hbar\omega_0}{T_L}\right) - 1}{1 + i_0 \frac{\Delta_i}{\hbar\omega_0} \frac{\tau_D}{\tau_0} \frac{T_0}{T_L} \left[ \exp\left(\frac{\hbar\omega_0}{T_L}\right) - 1 \right]} \right\}} \quad (10)$$

Here  $T_L$  obeys the following equation [see equation (5)]:

$$T_L = T_0 \left[ 1 + \beta i_0 \left( \frac{\Delta_i}{T_0} \right) \right], \quad (11)$$

where  $\beta = \bar{\Sigma}_0/\tau_0 C$ . In the case of an undoped GL,  $\mu_e = \mu_h$ , so that for  $2\mu = \mu_e + \mu_h$  one can obtain [with the same accuracy in deriving equation (9)]:

$$\exp\left(\frac{2\mu}{T}\right) \simeq 1 + i_0 \frac{\tau_A}{\tau_0}. \quad (12)$$

Equations (8) - (11) allow to find the the effective carrier and optical phonon temperatures,  $T$  and  $\Theta$ , as well as the lattice temperature  $T_L$  near the GL as functions of the dc injected current density for the IDLEs with different structural parameters.

Figure 2 shows the dependences of the effective temperatures of the carriers  $T$ , optical phonons, and lattice  $T_L$   $\Theta$  on the normalized injected current density  $i_0$  (i.e., actually on the injected power density  $\Delta_i j_0/e$ ) for different values of  $\tau_D/\tau_0$  calculated using equations (8) - (12). It is assumed that  $T_0 = 25$  meV,  $\hbar\omega_0 = 150$  meV,  $\Delta_i = 1240$  meV,  $\bar{\Delta}_i = 1210$  meV,  $C = 1$  kW/cm<sup>2</sup>K, and  $\beta \simeq 2.76 \times 10^{-2}$ .

Figure 3 shows  $T$ ,  $\Theta$ , and  $T_L$  versus the normalized injected current density  $i_0$  for  $\Delta_i = 1240$  meV,  $\bar{\Delta}_i = 1090$  and  $1210$  meV (corresponding to  $\tau_0/\tau_{cc} = 1 - 5$ ), assuming  $C = 1$  kW/cm<sup>2</sup>K. One can see that  $T$  at  $\bar{\Delta}_i = 1210$  meV only slightly exceeds  $T$  at  $\bar{\Delta}_i = 1090$  meV, while the values of  $\Theta$  for these cases are indistinguishable. As seen

from figure 3, the lattice temperature  $T_L$  is much lower than  $T$  and  $\Theta$  (for the chosen value of  $C$ ). The lattice temperature around of the GL is independent of  $\tau_D$ . As follows from equation (11) (and figure 3), it increases from  $T_L = 25$  meV (300 K) at  $i_0 = 0$  to  $T_L \simeq 59$  meV (about 710 K) at  $i_0 = 1$ , and to  $T_L \simeq 93$  meV (about 1116 K) at  $i_0 = 2$ . Hence, in the injected current densities range under consideration and the relatively high  $C$  characteristic for the hBNLs,  $T_L \simeq \hbar\omega_0$ . However, at small values of the hBNL thermal conductivity  $C$  (in the devices with far from ideal heat removal),  $T_L$  can be very close to  $\Theta$  and only slightly lower than  $T$ . Figure 4 shows  $T$ ,  $\Theta$ , and  $T_L$  calculated as functions of the hBNL thermal conductivity (i.e., the hBNL thickness). One can see that in a wide range of  $C$ , the temperatures  $T$ ,  $\Theta$ , and  $T_L$  fairly weakly depend on  $C$  in a wide range of its variation (at the given injection current densities). However, at small values of the hBNL thermal conductivity  $C$  (the devices with far from ideal thermal removal), the temperatures  $T$ ,  $\Theta$ , and  $T_L$  can become quite high with  $T_L$  being very close to  $\Theta$  and only slightly lower than  $T$ . The  $T$ ,  $\Theta$ , and  $T_L$  versus  $C$  relations are shown only in the range  $C$  ( $C \geq 0.10 - 0.17$  kW/cm<sup>2</sup>K) corresponding to  $T_L$  smaller than the hBNL melting temperature  $T_L \lesssim 250$  meV ( $T_L < 2973$  K).

### 3.2. Asymptotic analytic relations: weak heating

One can get analytic formulae for  $T$  and  $\Theta$  in the limits of small and relatively high injection currents. At small injected current densities  $j_0$  ( $i_0 \ll 1$ ), the temperatures  $T, \Theta, T_L \ll \hbar\omega_0$  and equation (10) yields

$$\Theta \simeq T_0 \left[ 1 + i_0 \frac{\Delta_i}{\hbar\omega_0} \frac{T_0}{\hbar\omega_0} \exp\left(\frac{\hbar\omega_0}{T_0}\right) \frac{\tau_D}{\tau_0} \right]. \quad (13)$$

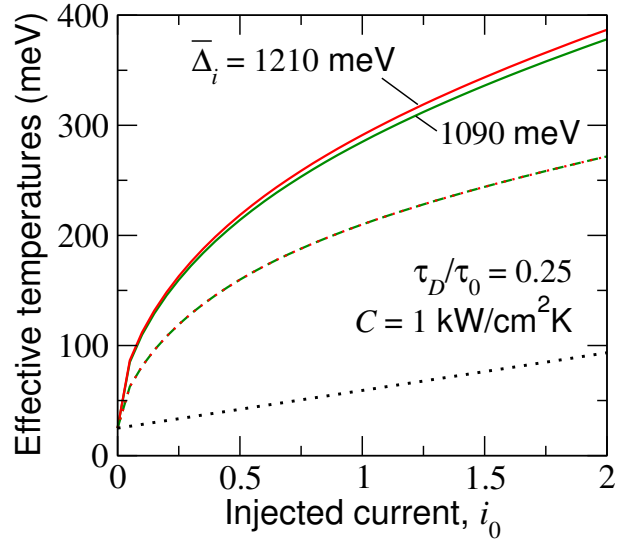


**Figure 3.** Effective carrier temperature  $T$  (solid lines), optical phonon temperature  $\Theta$  (dashed line), and lattice temperature  $T_L$  (dotted line) versus the injected current  $j_0$  for  $\tau_D/\tau_0 = 0.25$  at different  $\overline{\Delta}_i$ , setting  $\Delta_i = 1240$  meV,  $C = 1$  kW/cm<sup>2</sup>K, and  $T_0 = 25$  meV.

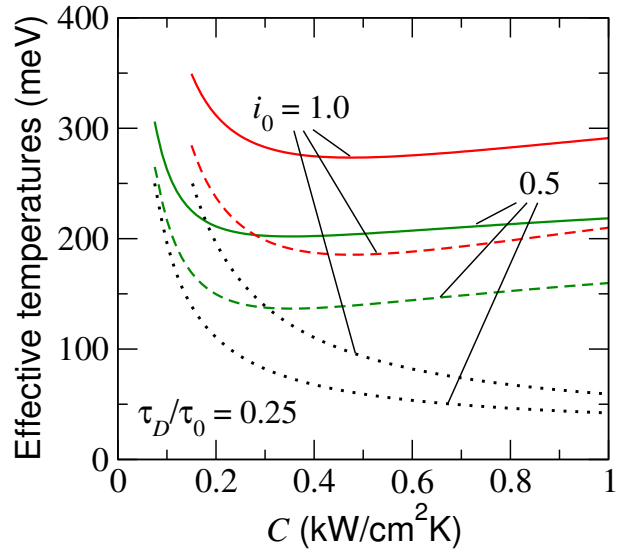


**Figure 4.** Effective carrier temperature  $T$  (solid lines), optical phonon temperature  $\Theta$  (dashed lines), and lattice temperature  $T_L$  (dotted lines) as functions of the hBNL thermal conductivity  $C$  at the injected current  $i_0 = 1$  and  $i_0 = 2$  for  $\Delta = 1240$  meV,  $\overline{\Delta}_i = 1210$  meV,  $\tau_D/\tau_0 = 0.25$ , and  $T_0 = 25$  meV.

As for the carrier effective temperature  $T$  at relatively low injection current, from equation (8) we obtain

$$T \simeq \Theta + T_0 \frac{i_0 \frac{\bar{\Delta}_i}{\hbar\omega_0} \left(\frac{T_0}{\hbar\omega_0}\right) \exp\left(\frac{\hbar\omega_0}{T_0}\right)}{\left[1 + \left(\frac{\pi T_0}{\hbar\omega_0}\right)^2\right]} \quad (14)$$

with  $\Theta$  given by equation (13). According to equation (14),  $T > \Theta$ . An increase in  $T$  with increasing injection current density is consistent with the energy relaxation on optical phonons in line with the previous results [18,70].

### 3.3. Asymptotic analytic relations: strong heating

At a strong injection (large  $i_0$ ), the 2DEP, optical phonon system and the lattice (near the GL) can be fairly hot. At large values of  $i_0$ , from equation (8) - (12) we obtain the following relations:

(A) High thermal conductivity  $C$  (small  $\beta$ ). In this case,

$$T_L \simeq T_0, \quad \Theta \simeq i_0 \Delta_i \frac{\tau_D}{\tau_0}, \quad (15)$$

$$T \simeq \frac{i_0 \Delta_i}{2} \left(\frac{\tau_D}{\tau_0}\right) \left[1 + \sqrt{1 + \frac{4}{\pi^2} \frac{\bar{\Delta}_i \hbar\omega_0}{\Delta_i} \left(\frac{\tau_0}{\tau_D}\right)^2 \frac{1}{i_0}}\right] \\ \simeq i_0 \Delta_i \left(\frac{\tau_D}{\tau_0}\right) + \frac{\hbar\omega_0}{\pi^2} \left(\frac{\tau_0}{\tau_D}\right) \left(\frac{\bar{\Delta}_i}{\Delta_i}\right). \quad (16)$$

(B) Low thermal conductivity  $C$  (large  $\beta$ ). In such a case,

$$T_L \simeq \beta i_0 \Delta_i, \quad \Theta \simeq \beta i_0 \Delta_i + \frac{T_0}{\beta} \frac{\tau_D}{\tau_0}, \quad (17)$$

$$T \simeq \frac{\beta i_0 \Delta_i}{2} \left[1 + \sqrt{1 + \frac{4}{\pi^2 \beta} \frac{\bar{\Delta}_i \hbar\omega_0}{\Delta_i} \left(\frac{\tau_0}{\tau_D}\right) \frac{1}{i_0}}\right] \\ \simeq \beta i_0 \Delta_i + \frac{\hbar\omega_0}{\pi^2} \left(\frac{\tau_0}{\tau_D}\right) \left(\frac{\bar{\Delta}_i}{\Delta_i}\right). \quad (18)$$

In the case "B",  $T \gtrsim \Theta \gtrsim T_L \gg T_0$  in agreement with the  $T$ ,  $\Theta$ , and  $T_L$  versus  $C$  relations shown in figure 4. Since  $T_L$  is limited by the hBNL melting temperature  $T_L^{melt}$ , equation (17) provides a limitation on  $i_0 < i_0^{melt} = T_L^{melt}/\beta\Delta_i$ . Setting  $T_L^{melt} \simeq 256$  meV ( $\sim 2973$  K),  $\Delta_i = 1240$  meV, and  $C = 0.1$  kW/cm<sup>2</sup>K ( $\beta = 2.76$ ), we find  $i_0^{melt} \simeq 0.74$ .

It is instructive that according to equations (15) - (18), both  $T$  and  $\Theta$  are linear functions of  $i_0$  when the latter is sufficiently large. In both cases "A" and "B", the difference  $T - \Theta$  [the second terms in the right-hand sides in equations (17) and (18)] is independent of  $i_0$ . As follows from the above equations that  $dT/di_0 > d\Theta/di_0$  in the range of small values of  $i_0$ , whereas  $dT/di_0 = d\Theta/di_0$  when  $i_0$  is large. The asymptotic relations of  $T$  and  $\Theta$  on  $i_0$  are in line with the above numerical data.

## 4. Steady-state spectral characteristic and output optical power

The probability,  $\nu_R$ , of the interband radiative transition in the GL is given by [71, 72]

$$\nu_R(p) = \frac{8}{3} \left(\frac{e^2 \sqrt{\kappa_{hBN}}}{\hbar c}\right) \left(\frac{v_W}{c}\right)^2 \frac{v_W p}{\hbar}. \quad (19)$$

Here  $\kappa_S$  is the dielectric constant of hBN,  $c$  is the speed of light in vacuum, and  $p = \hbar\omega/2c$  is the carrier momentum in the initial and final state, where  $\hbar\omega$  is the energy of the emitted photon. In the range of the photon frequencies ( $\omega > 1/\tau$ ) the processes associated with the indirect intraband transitions with the absorption (the Drude absorption) and emission of the photons are much weaker than the interband processes. Therefore, we account solely for the interband radiative transitions. Since the rate of the interband radiative transition [71, 72]

$$R_R(\hbar\omega) \propto (\mathcal{N}_{\hbar\omega} + 1) \times \nu_R(p) \Big|_{p=\hbar\omega/2c} f_e(\varepsilon_e) \Big|_{\varepsilon_e=\hbar\omega/2} f_h(\varepsilon_h) \Big|_{\varepsilon_h=\hbar\omega/2}, \quad (20)$$

where  $\mathcal{N}_{\hbar\omega} = \exp(\hbar\omega/T_0) - 1^{-1}$  is the distribution function of the photons in equilibrium with the thermostat, we arrive at the following expressions for the flux  $S_{\hbar\omega}$  (in units  $\text{cm}^{-2}\text{s}^{-1}$ ) and the output power  $P = A \int_0^\infty d(\hbar\omega) S_{\hbar\omega}$  (in units  $\text{W cm}^{-2}$ ) of the photons emitted by the GL(s):

$$S_{\hbar\omega} \simeq \frac{S_0 \left(\frac{\hbar\omega}{T_0}\right)^3 \exp\left(\frac{\hbar\omega}{T_0}\right)}{\left[1 + \zeta \exp\left(\frac{\hbar\omega}{2T}\right)\right]^2 \left[\exp\left(\frac{\hbar\omega}{T_0}\right) - 1\right]}, \quad (21)$$

$$P = S_0 T_0 \left(\frac{T}{T_0}\right)^4 \times \int_0^\infty \frac{dZ Z^3 \exp\left(Z \frac{T}{T_0}\right)}{\left[1 + \zeta \exp\left(\frac{Z}{2}\right)\right]^2 \left[\exp\left(Z \frac{T}{T_0}\right) - 1\right]}. \quad (22)$$

Here  $S_0 = \frac{2A}{3\pi} \left(\frac{e^2 \sqrt{\kappa_{hBN}} T_0^3}{\hbar^4 c^3}\right)$ ,  $\zeta = \exp(-\mu/T)$ , and  $A < 1$  is the fraction of the emitted photons not reflected by the outer surface. According to equation (11),  $\zeta = (1 + \beta i_0 \tau_A / \tau_0)^{-1/2}$ . For  $\sqrt{\kappa_{hBN}} \simeq 2.5$ ,  $T_0 = 25$  meV, and  $A \lesssim 1$  one obtains  $S_0 \simeq 3 \times 10^{17} \text{ cm}^{-2}\text{s}^{-1}$ .

In deriving equation (22), we have neglected the photon recycling and the photon accumulation inside the device (i.e., the resonant properties of the heterostructure). In the case of small  $(\mu_e + \mu_h)/T$ , equations (21) and (22) coincide with the pertinent formulae in our recent paper [46] [in which the injection of relatively low energy carriers was considered, so that  $(\mu_e + \mu_h)/T$  can be large].

Figure 5 shows the spectral dependence of the output radiation  $S_{\hbar\omega}$  for different

normalized injection current densities  $i_0$ . Figure 6 presents the output power  $P$  versus the normalized injection current density  $i_0$  for the same parameters as in figure 5. As follows from figures (5) and (6), the IDLEs can be effective sources of near-infrared and visible light.

The output radiation power as a function of the 2DEHP effective temperature  $T$  can be estimated by evaluating the integral in equation (22). As a result, we arrive at

$$P \simeq 5.24 \left(\frac{T}{T_0}\right)^4 \text{ mW/cm}^2. \quad (23)$$

The output power,  $P^{BB} = (\pi^2/60\hbar^3 c^2) T^4$ , of the thermal radiation emitted by a similar structure considered as the black-body with the same temperature  $T$  is given by

$$P_0^{BB} = \left(\frac{\pi^2}{60\hbar^3 c^2}\right) T_0^4 = 45.9 \text{ mW/cm}^2. \quad (24)$$

Comparing  $P$  and  $P^{BB}$ , given by equations (23) and (24), respectively, we obtain the following estimate for the IDLE emissivity:  $\epsilon_{GL} = P/P^{BB} \simeq 0.114$ . The latter is several times larger than that estimated in [48,49] and close to the value obtained in [46].

The power  $P_L^{GB}$ , emitted by the heated hBHL(s) considering it as a gray body with the emissivity  $\epsilon_{hBN}$  and setting that the average temperature  $\bar{T}_L = (T_L - T_0)/2$ , where  $T_L$  is given by equation (11), is estimated as

$$P_L^{GB} = \epsilon \left(\frac{\pi^2}{960\hbar^3 c^2}\right)^4 (\beta i_0 \Delta_i)^4. \quad (25)$$

For  $\Delta_i = 1240$  meV,  $C = 1 \text{ kW/cm}^2\text{K}$  ( $\beta = 0.0276$ ) and  $\epsilon = 0.1$ , equation (25) yields  $P_L^{GB} \simeq 1 \times i_0^4 \text{ mW/cm}^2$ . Taking into account that  $T > \bar{T}_L, T_L$ , we find  $P_L^{GB} \ll P$ . At low value of the thermal conductivity  $C$ , the lattice

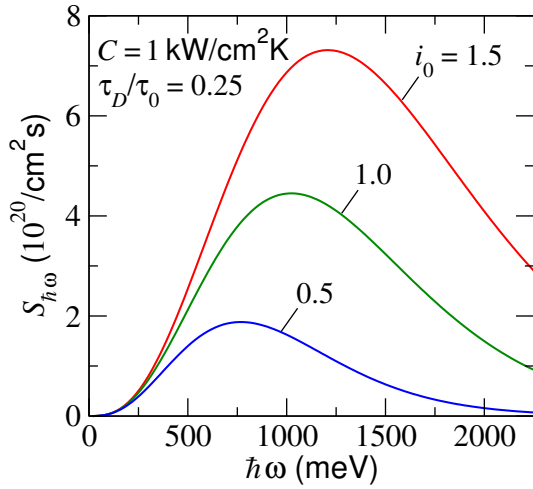


**Figure 5.** Emitted radiation spectral characteristic  $S_{h\omega}$  for different normalized injection current densities  $i_0$  ( $\Delta_i = 1210$  meV,  $\bar{\Delta}_i = 1210$  meV,  $\tau_D/\tau_0 = 0.25$ , and  $T_0 = 25$  meV).

can be strongly heated, so that  $\bar{T}_L \simeq T_L \simeq T$ , and the net emitted power can be fairly high being only limited by the melting of the device.

The emitted optical power is much larger than that in the case of "cold" injection [46], but the values of the emissivity are close in the IDLEs in question and in the source considered in [46], but the values of the emissivities of the IDLEs and of the source considered in [46] are close.

## 5. Dynamic response: modulation characteristics

We consider the temporal variations (modulation) of the applied voltage,  $U = U_0 + \delta U_m \exp(-i\omega_m t)$ , so that  $j = j_0 + \delta j_m \exp(-i\omega_m t)$ ,  $\delta i_m = \delta j_m/\bar{j}$ , where  $V_0$  and  $j_0$  are the dc bias voltage and current density,  $\delta V_m$  and  $\delta j_m$  are the pertinent amplitudes of the ac signal, and  $\omega_m$  is the modulation frequency.

In the most interesting situations when the modulation frequency  $\omega_m$  is sufficiently

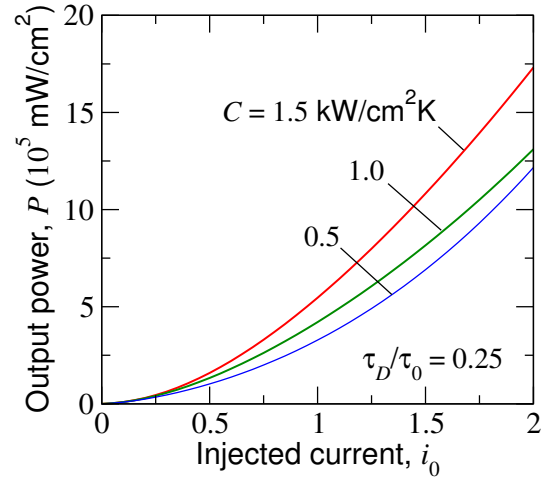


**Figure 6.** Output radiation power (per unit of square) as a function of normalized injection current densities  $i_0$  for different values of the thermal conductivity  $C$ . ( $\Delta_i = 1240$  meV,  $\bar{\Delta}_i = 1210$  meV,  $\tau_D/\tau_0 = 0.25$ , and  $T_0 = 25$  meV).

high [ $\omega_m \gg 1/\tau_L$ , see equation (5)], the lattice temperature  $T_L$  fails to follow the variations of the injected current. This implies that we can neglect the value  $\delta T_L$ . Taking this into account, from equation (4) we obtain

$$\delta \mathcal{N}_0 = \frac{\Delta_i}{\hbar\omega_0} \frac{\tau_D}{\tau_0} \frac{T_0}{T_L} \frac{\delta i_m}{(1 - i\omega_m \tau_D T_0/T_L)}. \quad (26)$$

If

$$\frac{\tau_D}{\tau_0} \frac{T_0}{T_L} = \frac{\tau_D}{\tau_0} \frac{1}{1 + \beta i_0 (\Delta_i/T_0)} \ll 1,$$

(i.e., at a relatively small  $\tau_D$  and not too small injection current densities), the variation of  $T$  is larger than the variation of  $\mathcal{N}_0$ . Assuming the latter for the subsequent formulae brevity, we found from equation (2)

$$\begin{aligned} -i\omega_m \left( \frac{\partial \mathcal{E}}{\partial T} \right) \delta T_m &\simeq \frac{\delta j_m \bar{\Delta}_i}{e} \\ -\hbar\omega_0 \left( \frac{\partial R_0^{inter}}{\partial T} + \frac{\partial R_0^{intra}}{\partial T} \right) \delta T_m. \end{aligned} \quad (27)$$

Here the terms in the brackets are taken at the steady-state values of  $T$  and  $\mathcal{N}_0$ . Considering

equation (8) and equation (2) with  $\mathcal{E}$  given by (see the Appendix)

$$\mathcal{E} \simeq \nu \Sigma_0 \left( \frac{T}{T_0} \right)^2 T, \quad (28)$$

with the coefficient  $\nu \simeq 2.19$ , when  $T$  is a relatively large ( $T \gtrsim \hbar\omega_0$ , i.e.  $T \gtrsim 1800$  K), we arrive at the following rough estimate for the effective carrier temperature:

$$\frac{|\delta T_m|}{T} \sim \frac{|\delta j_m|}{2j_0} \frac{1}{\sqrt{(1 + \omega_m^2 \tau_T^2)}}, \quad (29)$$

where  $\tau_T \simeq \frac{\nu\tau_0}{2} \left( \frac{\pi T}{\hbar\omega_0} \right)^2 \left( \frac{T}{\Delta_i} \right)$ . At  $T = (290 - 370)$  meV ( $i_0 = 1 - 2$ , see figures 2 and 3) one obtains  $\tau_T \simeq 10 - 20$  ps, For the pertinent modulation cut-off frequency  $f_m^{max}$ , defined as  $1/\sqrt{1 + (2\pi f_m^{max} \tau_T)^2} = \sqrt{2}/2$ , we find  $f_m^{max} \simeq (8 - 16)$  GHz. The latter values of  $f_m^{max}$  are in line with the recent predictions for the GL-based light emitter with the Joule heating [55] and much larger than those in an earlier work [73].

Using equation (27) for  $\delta T_m$  and equation (22) for the output optical power, we obtain the following estimate for the radiation modulation depth  $\delta P_m$ :

$$\frac{\delta P_m}{P} \simeq \frac{4|\delta T_m|}{T} \simeq \frac{2\delta j_m}{j_0} \frac{1}{\sqrt{(1 + \omega_m^2 \tau_T^2)}}. \quad (30)$$

The power modulation depth described by equation (30) is much larger than for the devices in which the electron and lattice temperatures are close. The latter one applies to the IDLEs with the weak remove of the lattice heat (small  $C$ , large  $\beta$ ). This is because when the steady state temperatures  $T \sim T_L$ , the thermal emission of the lattice (as a gray body system) makes the denominator in equation (30) too large, while  $|\delta T_m| \gg |\delta T_L|$ .

This emphasizes the necessity to provide a high thermal conductance of the hBNLs and of the top metal contact serving as effective heat sinks. A similar situation takes place in the standard incandescent lamps.

## 6. Injected current-voltage characteristics

The injected current density  $j$  is determined by the voltage  $U$  applied between the n<sup>+</sup>-side contacts to the GL(s) and the p<sup>+</sup>-region of the vertical contact (see figure 1). When  $U < U_{bi}$ , where  $eU_{bi} \sim \Delta_G^{hBN}$  is the built-in voltage and  $\Delta_G^{hBN}$  is the hBNL energy gap [as shown in figures 1(c) and 1(d)], the hole injection into the GL(s) is controlled by the energy barrier at the p-hBNL/GL interface. High carrier densities in the GL(s) result in high efficiency of the carrier-carrier scattering, and, therefore, the injected holes are more likely to be captured into the GL(s) than rejected back to the injector. This is in contrast to the situations in the standard quantum-well and GL-based structures [74, 75] with the injected carriers mainly passing across such structures, in which the capture probability is relatively small. Hence, in the IDLEs under consideration, the density of the injection current to a single- or multiple-GL is given by

$$j_i = j^{max} \exp \left[ \frac{e(U - U_{bi})}{T_0} \right]. \quad (31)$$

Here  $j^{max} = eN^+v_T$  with  $N^+$  and  $v_T$  being the hole density in the p<sup>+</sup>-contact region and the hole thermal velocity, respectively. For an effective 2DEHP heating ( $i_0 \gtrsim 1 - 2$ ) the injected current density  $j_i$  should exceed  $n\bar{j} = e\bar{\Sigma}_0/\tau_0$ , where  $n$  is the number of the GLs in the device. Assuming the latter be equal to  $\bar{j} = 320$  kA/cm<sup>2</sup> (see section 3), we arrive at the following condition:  $N^+ \gtrsim 2n \times 10^{17}$  cm<sup>-2</sup>.

Taking into account the energy of the injected holes, we estimate the injected power density  $P_i$  for  $i_0 = 0.5 - 2.0$ :  $P_i \simeq 200 - 800 \text{ kW/cm}^2$ . These values of the injected power density are of the same order of magnitude as, for example, in [55].

Equations (30) and (31) yield

$$\frac{\delta P_m}{P} \simeq \frac{2e\delta U_m}{T_0} \frac{1}{\sqrt{(1 + \omega_m^2 \tau_T^2)}}. \quad (32)$$

## 7. Comments

Depending on the contact metal, roughness of of its surface and the surrounding air pressure,  $C$  and  $\beta$  can be in ranges of (1 - 15) W/cm<sup>2</sup>K and 2 - 30, respectively. However, in the latter case, the IDLE energy balance essentially depends on the radiated power [50], which is disregarded in our model.

Similar IDLEs can exploit the lateral hole injection combined with the vertical electron injection. In this case, the electrons captured into the GL acquire the energy  $\Delta_C$ , so that in the above equations one needs to put  $\Delta_i \simeq \Delta_C + 3T_0/2$ . Due to  $\Delta_C > \Delta_V$  at the hBNL/GL interface, a relatively strong 2DEHP heating can occur at markedly smaller injection current densities. Analogously, in the IDLEs with the vertical double injection of both the electrons and holes [see Figure 1(b) and 1(d)], the quantity  $\Delta_i$  can be larger:  $\Delta_i \simeq \Delta_C + \Delta_V + 3T_0 \gtrsim \Delta_G^{hBN}$ . However, in this case,  $\bar{\Delta}_i$  can be markedly smaller than  $\Delta_i$  because of a larger factor  $k_0$  in equation (3).

The operation of the IDLSs under consideration is associated with the injection of rather hot carriers. This is in contrast to the thermal light emitters using the double injection of relatively cold carriers, which are heated by the lateral current (via the Joule heating). The comparison of the IDLE under

consideration and the emitters using the Joule heating (for example, [54, 55]) demonstrates comparable or better characteristics (the consumed power and the emission efficiency) of the former. An advantage of the IDLEs can be associated with more uniform spatial distribution of the injected power in comparison with the devices with the Joule heating. In the latter, the Joule power cannot be distributed along the GL fairly uniformly due to the essential non-linearity of the lateral current-voltage characteristics [48, 76]. Also, the in the emitter with the Joule heating having a short GL, the hot carrier can quickly pass through the GL and release a substantial power in the collecting contacts. The IDLEs can exhibit higher modulation efficiency due to higher values of  $\delta j_m / \delta U_m$ . This is because in the case of the lateral Joule heating, the injected current as a function of the applied voltage tends to saturation [55] (see also [76]) that results in smaller  $\delta j_m / \delta U_m$ .

The developed IDEL mathematical model can also be applied for more detailed analyzing of the thermal light sources using other method of the carrier heating, including those with the Joule heating.

## 8. Conclusions

The transparent mathematical model of the proposed IDLEs using the combined lateral-vertical carrier injection into the GL(s) encapsulated by the hBNLs allows to analyse, evaluate, and optimize the device characteristics.

The device model under consideration showed that the IDLEs can serve as simple efficient light emitters. Due to the possibility of fast variations of the hot carrier injection and temperature by varying voltage, these emitters can generate near-infrared and visible light modulated in the GHz range that is not

possible for the standard incandescent lamps. This feature enables IDLEs can be used in different communication and signal processing optoelectronic systems.

## Acknowledgments

One of the co-authors (VR) is grateful to Prof. Yu. G. Gurevich (Mexico) for fruitful discussion.

This work was supported by the Japan Society for Promotion of Science (KAKENHI #16H06361), Japan; the Russian Foundation for Basic Research (Grants # 18-29-02089, # 18-07-01379), Russia; RIEC Nation-Wide Cooperative Research Project #H31/A01), Japan. The work at RPI was supported by the US Army Research Laboratory Cooperative Research Agreement (Project Monitor Dr. Meredith Reed) and by the US Office of Naval Research (Project Monitor Dr. Paul Maki), USA.

## Appendix. General equations

### 1. Interband and intraband transitions rates

The rates of the interband and intraband processes involving the optical phonons can be presented as:

$$R_0^{inter} = \frac{\bar{\Sigma}_0}{\tau_0} \times \left[ (\mathcal{N}_0 + 1) \exp\left(\frac{\mu_e + \mu_h - \hbar\omega_0}{T}\right) - \mathcal{N}_0 \right], \quad (\text{A1})$$

$$R_0^{intra} = \frac{\bar{\Sigma}_0}{\tau_0 \eta_0} \left[ (\mathcal{N}_0 + 1) \exp\left(-\frac{\hbar\omega_0}{T}\right) \right] - \mathcal{N}_0 \quad (\text{A2})$$

Here  $G_0 = (\bar{\Sigma}_0/\tau_0) \exp(-\hbar\omega_0/T_0)$  is the rate of the electron-hole pair generation due to the absorption of equilibrium optical phonons and  $\eta_0 = \hbar^2\omega_0^2/\pi^2T^2$  characterizes

the effect of the density of states in GLs on the interband and intraband optical phonon mediated transitions [58]. At  $T_0 = 25$  meV, for the intra-valley optical phonons in GLs,  $G_0 \simeq 10^{21} \text{ cm}^{-2}\text{s}^{-1}$  [60].

Considering the contribution of both the intra-valley and inter-valley optical phonons [60] as well as the interface optical phonons, we set  $G_0 \simeq 4 \times 10^{21} \text{ cm}^{-2}\text{s}^{-1}$ . Setting  $\hbar\omega_0 = 150$  meV, we obtain the density of the hole states in GLs (involved in the optical phonon absorption)  $\bar{\Sigma}_0 = (2/\pi\hbar^2v_W^2) \int_0^{\hbar\omega_0} d\varepsilon \varepsilon = (1/\pi)(\hbar\omega_0/\hbar v_W)^2$ , we obtain  $\bar{\Sigma}_0 \simeq 1.83 \times 10^{12} \text{ cm}^{-2}$ . Consequently, for the optical phonon spontaneous emission:  $\tau_0 = (\bar{\Sigma}_0/G_0) \exp(-\hbar\omega_0/T_0) \simeq 1.1$  ps. The ratio  $\bar{\Sigma}_0/\Sigma_0$ , where  $\Sigma_0 = (\pi/3)(T_0/\hbar v_W)^2$ , which is the carrier density in the 2DEHP in equilibrium, is equal to  $3(\hbar\omega_0/\pi T_0)^2 \simeq 10.9$ .

The Auger recombination-generation term in equation (1) can be presented in the following simplified form (see, for example, [11]):

$$R_A \simeq \frac{\bar{\Sigma}_0}{\tau_A} \left[ \exp\left(\frac{\mu_e + \mu_h}{T}\right) - 1 \right]. \quad (\text{A3})$$

The Auger mechanisms in GLs are very specific due to the linear gapless electron and hole dispersion law, which formally prohibits the recombination-generation processes with the participation of two electrons and one hole and two holes and one electron [65]. However, the Auger processes, involving other scatterers and affected by the dynamic screening of the carrier interactions and renormalization of the carrier energy spectra, can be essential. Moreover, the characteristic time of the Auger recombination in GLs  $\tau_A$ , being relatively long at moderate carrier densities and temperatures, can be fairly short for the high densities and temperatures. Indeed, as a thorough study shows [58],  $\tau_A \simeq 1.1$  ps at  $T = 300$  K in the GL encapsulated

by the hBNLs, but  $\tau_A \simeq 0.07 - 0.2$  ps at  $T = 1000 - 3000$  K. This implies that in the IDLEs, which can be effective just in the latter carrier effective temperature range, we can assume (in contrast to some devices considered previously) that  $\tau_A$  is smaller than  $\tau_0$ . The carrier-carrier scattering leads to the effective carrier temperature common for the electrons and holes. The Auger recombination-generation processes tend to equilibrate the electrons and holes aligning their quasi-Fermi levels. Such an equilibrium (apart from the equality of the electron and hole effective temperatures) corresponds to  $\mu_e = -\mu_h = \mu$ , i.e.,  $\mu_e + \mu_h = 0$ . In the case of undoped GLs, the latter implies  $\mu_e = \mu_h = \mu = 0$ .

If  $\tau_A$  is small, it follows from equation (1) with equations (A1) and (A2) that  $2\mu/T = (\mu_e + \mu_h)/T$  is also small that leads to

$$R_0^{inter} = \frac{\overline{\Sigma_0}}{\tau_0} \left[ (\mathcal{N}_0 + 1) \exp\left(-\frac{\hbar\omega_0}{T}\right) - \mathcal{N}_0 \right], \quad (\text{A4})$$

$$R_0^{inter} + R_0^{intra} = \frac{\overline{\Sigma_0}}{\tau_0} \left( 1 + \frac{1}{\eta_0} \right) \times \left[ (\mathcal{N}_0 + 1) \exp\left(-\frac{\hbar\omega_0}{T}\right) - \mathcal{N}_0 \right]. \quad (\text{A5})$$

Considering that, at the IDLE operation conditions the Auger recombination time  $\tau_A$  is fairly small and expressing the quantity  $\exp[(\mu_e + \mu_h)/T]$  via  $i_0$ , from equation (6) we obtain

$$\left( 1 + \frac{1}{\eta_0} \right) \left[ (\mathcal{N}_0 + 1) \exp\left(-\frac{\hbar\omega_0}{T}\right) - \mathcal{N}_0 \right] = i_0 \left[ \frac{\overline{\Delta_i}}{\hbar\omega_0} - (\mathcal{N}_0 + 1) \exp\left(-\frac{\hbar\omega_0}{T}\right) \frac{\tau_A}{\tau_0} \right]. \quad (\text{A6})$$

## 2. Carriers thermal energy and their heat capacitance

The density of the carrier energy in the 2DEHP can be calculated as

$$\begin{aligned} \mathcal{E} &= \frac{2T^3}{\pi\hbar^2 v_W^2} \int_0^\infty dz z^2 \\ &\times \left[ \frac{1}{1 + \exp\left(z - \mu_e/T\right)} + \frac{1}{1 + \exp\left(z - \mu_h/T\right)} \right] \\ &\simeq \frac{2T^3}{\pi\hbar^2 v_W^2} \left( 3\zeta(3) + 1.64 \frac{\mu_e + \mu_h}{T} \right) \\ &\simeq \nu \Sigma_0 T \left( \frac{T}{T_0} \right)^2, \end{aligned} \quad (\text{A7})$$

where  $\nu = 18\zeta(3)/\pi^2 \simeq 6 \cdot 3.61/\pi^2 \simeq 2.19$  and  $\zeta(x)$  is the Rieman zeta-function.

At  $|\mu_e + \mu_h| \ll T$ , equation (A7) yields the following value of the 2DEHP specific heat capacitance per unit of the 2DEHP area:

$$C_c = 3\nu \Sigma_0 \left( \frac{T}{T_0} \right)^2 = \pi\nu \left( \frac{T}{\hbar v_W} \right)^2, \quad (\text{A8})$$

where  $c_c = 3\nu \simeq 6.57$  stands for the carrier heat capacitance per one carrier.

The carrier specific heat capacitance per unit area  $C_c = c_c \Sigma_0 (T/T_0)^2$  is small compared with the specific lattice heats of the GLs and hBNLs. However,  $C_c$  determines the high-speed modulation characteristic (the maximum modulation frequency  $f_m^{max} \propto C_c$ ) since, in this case, the lattice temperature does not follow the external modulation signals.

## 3. Distribution of the injected energy between the 2DEHP and the optical phonon system

Considering the cascade of optical phonons emitted by the injected holes, one can estimate the fractions of the power,  $\hbar\omega_0 k_0 / \Delta_i$ , which directly transferred to the optical phonon systems, invoking the following formula:

$$\begin{aligned} k_0 &= \sum_{n=1}^{K_0} \frac{1}{(1 + \tau_0/\tau_{cc})^n} \\ &= \frac{1}{\tau_0/\tau_{cc}} \left[ 1 - \frac{1}{(1 + \tau_0/\tau_{cc})^{K_0}} \right] \end{aligned} \quad (\text{A9})$$

with  $K_0$  being the number of the pertinent optical phonons in the cascades. In the case of small  $\tau_0/\tau_{cc}$ , equation (A9) can be presented as  $k_0 \simeq K_0/(1 + K_0\tau_0/\tau_{cc})$ .

Equation (A9) ignores the dependence of  $\tau_0$  on the injected hot hole energy. In the case when  $\tau_0$  is proportional to the hole energy, one can obtain the following formula replacing equation (A9):

$$\begin{aligned} k_0 &= \frac{1}{[1 + \tau_0/K_0\tau_{cc}]} \\ &+ \frac{1}{[1 + \tau_0/K_0\tau_{cc}][1 + \tau_0/(K_0 - 1)]} + \dots \\ &= \frac{K_0}{1 + \tau_0/\tau_{cc}}. \end{aligned} \quad (\text{A10})$$

- [1] Xia F, Mueller T, Lin Y M, Valdes-Garsia A and Avouris P 2009 Ultrafast graphene photodetector *Nat. Nanotechnol.* **4** 839 - 843.
- [2] Ryzhii V, Ryzhii M, Mitin V and Otsuji 2009 Terahertz and infrared photodetectors using p-i-n multiple-graphene structures *J. Appl. Phys.* **106** 084512.
- [3] Ryzhii V, Ryabova N, Ryzhii M, Baryshnikov N, Karasik V, Mitin V and Otsuji 2011 Terahertz and infrared photodetectors based on multiple graphene layer and nanoribbon structures *Opto-Electronics Review* **20** 15 - 25.
- [4] Bonaccorso F, Sun Z, Hasan T and Ferrari A C 2010 Graphene photonics and optoelectronics *Nat. Photon.* **4** 611.
- [5] Gan X, Shiue R-J, Gao Y, Meric I, Heinz T F, Shepard K, Hone J, Assefa S and Englund D 2013 Chip-integrated ultrafast graphene photodetector with high responsivity *Nat. Photonics* **7** 883 - 887.
- [6] Muraviev A V, Rumyantsev S L, Liu G, Balandin A A, Knap W and Shur M S 2013 Plasmonic and bolometric terahertz detection by graphene field-effect transistor *Appl. Phys. Lett.* **103** 181114.
- [7] Tredicucci A and M. S. Vitiello M S 2014 Device concepts for graphene-based terahertz photonics *IEEE J. Sel. Top. Quantum Electron.* **20** 8500109.
- [8] Koppens F H L, Mueller T, Avouris P, Ferrari A C, Vitiello M S and Polini M 2014 Photodetectors based on graphene, other two-dimensional materials and hybrid systems *Nat. Nanotech.* **9** 780.
- [9] Ryzhii V, Otsuji T, Aleshkin V Ya, Dubinov A A, Ryzhii M, Mitin V and Shur M S 2014 Voltage-tunable terahertz and infrared photodetectors based on double-graphene-layer structures *Appl. Phys. Lett.* **104** 163505.
- [10] Ryzhii V, Ryzhii M, Svintsov D, Leiman V, Mitin V, Shur M S and Otsuji T. 2017 Infrared photodetectors based on graphene van der Waals heterostructures *Inf. Phys. Technol.* **84** 72 - 81.
- [11] Ryzhii V, Ponomarev D S, Ryzhii M, Mitin V, Shur M S and Otsuji T 2019 Negative and positive terahertz and infrared photoconductivity in uncooled graphene *Opt. Mat. Express* **9** 585 - 597.
- [12] Ryzhii V, Ryzhii M, Mitin V, Shur M S and Otsuji T 2020 Far-infrared photodetectors based on graphene/black-AsP heterostructures *Opt. Express* **28** 2480 - 2498.
- [13] Ryzhii V, Otsuji T, Karasik V E, Ryzhii M, Leiman V G, Mitin V and Shur M S 2018 Comparison of Intersubband Quantum-Well and Interband Graphene-Layer Infrared Photodetectors *IEEE J. Quantum Electron* **54** 4000108.
- [14] Ryzhii V, Ryzhii M, Ponomarev D S, Leiman V G, Mitin V, Shur M S and Otsuji T 2019 Negative photoconductivity and hot-carrier bolometric detection of terahertz radiation in graphene-phosphorene hybrid structures *J. Appl. Phys.* **125** 151608.
- [15] Gan X, Shiue R-J, Gao Y, Mak K-F, Yao X, Li L, Szep S, Walker D, Hone J, Heinz T F and Englund D 2013 High-contrast electrooptic modulation of a photonic crystal nanocavity by electrical gating of graphene *Nano Lett.* **13** 691 - 696.
- [16] Phare C T, Daniel Lee Y-H, Cardenas J and Lipson M 2015 Graphene electro-optic modulator with 30 GHz bandwidth *Nat. Photonics* **9** 511 - 514.
- [17] Ryzhii V, Otsuji T, Ryzhii M, Leiman V G, Yurchenko S O, Mitin V and Shur M S 2012 Effect of plasma resonances on dynamic characteristics of double graphene-layer optical modulator *J. Appl. Phys.* **112** 104507.
- [18] Ryzhii V, Otsuji T, Ryzhii M, Ponomarev D S, Karasik V E, Leiman V G, Mitin V and Shur M S 2018 Electrical modulation of terahertz radiation using graphene-phosphorene heterostructures *Semicond. Sci. Technol.* **33** 124010.
- [19] Ryzhii V, Satou and Otsuji T 2007 Plasma waves in two-dimensional electron-hole system in gated graphene heterostructures *J. Appl. Phys.* **101**

- 024509.
- [20] Grigorenko A N, Polini M and Novoselov K S 2012 Graphene plasmonics Nat. Photonics **6** 749 - 758.
- [21] Bao Q and Loh K P 2012 Graphene photonics, plasmonics, and broadband optoelectronic devices ACS Nano **6** 3677.
- [22] Low T and Avouris P 2014 Graphene plasmonics for terahertz to mid-infrared applications ACS Nano **8** 1086 - 1101.
- [23] Ryzhii V, Ryzhii M, Shur M S, Mitin V, Satou A and Otsuji T 2016 Resonant plasmonic terahertz detection in graphene split-gate field-effect transistors with lateral p-n junctions J. Phys. D **49** 315103.
- [24] Zhang Yu-P, Liu Ya-Q, Cao Y-Y, Lv H-H, Li T-T, Huang X, Zhang H-Y and Ren G-J 2015 Gain characteristics of THz surface plasmons in electrically pumped monolayer graphene Eur. Phys. J. Appl. Phys. **69** 10803.
- [25] Woessner A, Gao Y, Torre I, Lindberg M B, Tan C, Watanabe K, Taniguchi T, Hillenbrand R, Hone J, Polini M and Koppens F H L 2017 Electrical  $2\pi$  phase control of infrared light in a 350-nm footprint using graphene plasmons Nat. Photonics **11** 421 - 424.
- [26] Ryzhii V, Ryzhii M, Mitin V, Shur M S, Satou A and Otsuji T 2013 Terahertz photomixing using plasma resonances in double-graphene layer structures J. Appl. Phys. **113** 174506.
- [27] Dubinov A A, Aleshkin V Ya, Mitin V, Otsuji T and Ryzhii V 2011 Terahertz surface plasmons in optically pumped graphene structures J. Phys.: Cond. Mat. **23** 145302.
- [28] Ryzhii V, Otsuji T and Shur M S 2020 Graphene based plasma-wave devices for terahertz applications Appl. Phys. Lett. **116** 140501.
- [29] Ryzhii V, Ryzhii M and Otsuji T 2007 Negative dynamic conductivity of graphene with optical pumping J. Appl. Phys. **101** 083114.
- [30] Ryzhii V, Dubinov A, Otsuji T, Mitin V and Shur M S 2010 Terahertz lasers based on optically pumped multiple graphene structures with slot-line and dielectric waveguides J. Appl. Phys. **107** 054505.
- [31] Ryzhii V, Ryzhii M, Mitin V and Otsuji T 2011 Toward the creation of terahertz graphene injection laser J. Appl. Phys. **110** 094503.
- [32] Boubanga-Tombet S, Chan S, Watanabe T, Satou A, Ryzhii V and Otsuji T 2012 Ultrafast carrier dynamics and terahertz emission in optically pumped graphene at room temperature Phys. Rev. B **85** 035443.
- [33] Otsuji T, Boubanga Tombet S, Satou A, Ryzhii M and Ryzhii V 2013 Terahertz wave generation using graphene: toward new types of terahertz lasers IEEE J. Sel. Top. Quantum Electron. **19** 8400209.
- [34] Li T, Luo L, Hupalo M, Zhang J, Tringides M C, Schmalian J and Wang J 2012 Femtosecond population inversion and stimulated emission of dense Dirac fermions in graphene Phys. Rev. Lett. **108** 167401.
- [35] Gierz I, Petersen J C, Mitrano M, Cacho C, Turcu I E, Springate, Stöhr A, Köhler A, Starke U and Cavalleri A 2013 Snapshots of non-equilibrium Dirac carrier distributions in graphene Nat. Mater. **12** 1119.
- [36] Davoyan A R, Morozov M Yu, Popov V V, Satou A and Otsuji T 2013 Graphene surface emitting terahertz laser: diffusion pumping concept Appl. Phys. Lett. **103** 251102.
- [37] Yadav D, Boubanga Tombet S, Watanabe T, Arnold S, Ryzhii V and Otsuji T 2016 Terahertz wave generation and detection in double-graphene layered van der Waals heterostructures 2D Materials **2** 045009.
- [38] Yadav D, Tamamushi G, Watanabe T, Mitsushio J, Tobah Y, Sugawara K, Dubinov A A, Satou A, Ryzhii M, Ryzhii V and Otsuji T 2018 Terahertz light-emitting graphene-channel transistor toward single-mode lasing Nanophotonics **7** 741.
- [39] Kuruvila A, Kidambi P R, Kling J, Wagner J B, Robertson J, Hofmann S and Meyer J 2014 Organic light emitting diodes with environmentally and thermally stable doped graphene electrodes J. Mat. Chem. C **2** 6940 - 6945.
- [40] Withers F, Del Pozo-Zamudio O, Mishchenko A, Rooney A P, Gholinia A, Watanabe K, Taniguchi T, Haigh S J, Geim A K, Tartakovskii A and Novoselov K S 2015 Light-emitting diodes by bandstructure engineering in van der Waals heterostructures Nature Mater. **14** 301-306.
- [41] Jiang G, Tian He, Wang X-F, Hirtz T, Wu F, Quao Y-C, Gou G-Y, Yu-H, Wei Yu-H, Yang J-M, Yang S, Yang Yi and Ren T-L 2019 An efficient flexible graphene-based light-emitting device Nanoscale Adv. **1** 4745 - 4754.
- [42] Zheng J, Hoh H Y, Zhang Y, and Bao Q, Graphene-based light-emitting diodes in *Graphene Photonics, Optoelectronics, and Plasmonics* Q. Bao, H. Hoh, Y. Zhang eds., Chapter

- 9 (Jenny Stanford Publ., New York, 2017).
- [43] Palacios-Berraquero C, Barbone M, Kara D M, Chen X, Goykhman I, Yoon D, Ott A K, Beitner J, Watanabe K, Taniguchi T, Ferrari A C and M Atatüre M 2016 Atomically thin quantum light-emitting diodes *Nature Commun.* **7** 12978.
- [44] Ryzhii V, Ryzhii M, Otsuji T, Karasik V E, Leiman V, Mitin V, and Shur M S, 2020 Multiple graphene-layer-based heterostructures with van der Waals barrier layers for terahertz superluminescent and laser diodes with lateral/vertical injection *Semicond. Sci. Technol.* **35** no. 8.
- [45] Ryzhii V, Otsuji T, Ryzhii M, Karasik V E, and Shur M S 2019 Negative terahertz conductivity and amplification of surface plasmons in graphene-black phosphorus injection laser heterostructures *Phys. Rev. B* **100** 115436.
- [46] Ryzhii V, Ryzhii M, Maltsev P P, Karasik V E, Mitin V, Shur M S and Otsuji T 2020 Far-infrared and terahertz emitting diodes based on graphene/black-P and graphene/MoS<sub>2</sub> heterostructures *Opt. Express* **28** 24136 - 24151.
- [47] Zhou Z, Yin B and Michel J 2015 On-chip light sources for silicon photonics *Light Sci. Appl.* **4** e358.
- [48] Freitag M, Chiu H-Y, Steiner M, Perebeinos V and Avouris P 2010 Thermal infrared emission from biased graphene *Nat. Nanotech.* **5** 497 - 501.
- [49] Kim Y D, Kim H, Cho Y, Ryoo Ji H, Park C-H, Kim P, Kim Y S, Lee S, Li Y, Park S-N, Yoo Y S, Yoon D, Dorgan V E, Pop E, Heinz T F, Hone J, Chun S-H, Cheong H, Lee S W, Bae M-Ho and Park Y D 2015 Bright visible light emission from graphene *Nat. Nanotech.* **10** 676 - 681.
- [50] Barnard H R, Zossimova E, Mahlmeister N H, Lawton L M, Luxmoore I J and Nash G R 2016 Boron nitride encapsulated graphene infrared emitters *Appl. Phys. Lett.* **108** 131110.
- [51] Son S-K, Šiškins M, Mullan C, Yin J, Kravets V G, Kozikov A, Ozdemir S, Alhazmi M, Holwill M, Watanabe K, Taniguchi T, Ghazaryan D, Novoselov K S, Fal'ko V I and Mishchenko A 2017 Graphene hot-electron light bulb: incandescence from hBN encapsulated graphene in air *2D Materials* **5** 011006.
- [52] Dong H M, Xu W and Peeters F M 2018 Electrical generation of terahertz blackbody radiation from graphene *Opt. Express* **26**(19) 24621 - 24626.
- [53] Shiue R-J, Gao Y, Tan C, Peng C, Zheng J, Efetov D K, Kim Y D, Hone J and Englund D 2019 Thermal radiation control from hot graphene electrons coupled to a photonic crystal nanocavity *Nat. Commun.* **10** 109.
- [54] Luo F, Fan Y, Peng G, Xu S, Yang Y, Yuan K, Liu J, Ma W, Xu W, Zhu Z H, Zhang X-Ao, Mishchenko A, Ye Yu, Huang H, Han Z, Ren W, Novoselov K S, Zhu M and Qin S 2019 Graphene thermal emitter with enhanced Joule heating and localized light emission in air *ACS Photonics* **6** 2117 - 2125.
- [55] Kim Y D, Gao Y, Shiue R-J, Wang L, Aslan O B, Bae M-ho, Kim H, Seo D, Choi H-J, Kim S H, Nemilensau A, Low T, Tan C, Efetov D K, Taniguchi T, Watanabe K, Shepard K L, Heiz T F, Englund D and Hone J 2018 Ultrafast graphene light emitters *Nano Lett.* **18** 934 - 940.
- [56] Ling Xi, Wang H, Huang S, Xia F and Dresselhaus M S 2015 The renaissance of black phosphorus *PNAS* **112** 4523.
- [57] Cai Y, Zhang G and Zhang Y-W 2014 Layer-dependent band alignment and work function of few-layer phosphorene *Sci. Reports* **4** 6677.
- [58] Alymov G, Vyurkov V, Ryzhii V, Satou A and Svintsov D 2018 Auger recombination in Dirac materials: A tangle of many-body effects *Phys. Rev. B* **97** 205411.
- [59] Ryzhii V, Ryzhii M, Mitin V, Satou A and Otsuji T 2011 Effect of heating and cooling of photogenerated electron-hole plasma in optically pumped graphene on population inversion *Jpn. J. Appl. Phys.* **50** 094001.
- [60] Rana F, George P A, Strait J H, Sharavaraman S, Charasheyhar M and Spencer M G 2009 Carrier recombination and generation rates for intravalley and intervalley phonon scattering in graphene *Phys. Rev. B* **79** 115447.
- [61] Bonini N, Lazzeri M, Marzari N and Mauri F 2007 Phonon anharmonicities in graphite and graphene *Phys. Rev. Lett.* **99** 176802.
- [62] Wang H, Strait J H, George P A, Shivaraman S, Jahan Dawlaty, Shields V B, Chandrashekhara Mvs, Hwang J, Rana F, Spencer M G, Ruiz-Vargas C S and Park J 2010 Ultrafast relaxation dynamics of hot optical phonons in graphene *Appl. Phys. Lett.* **96** 081917.
- [63] Kang K, Abdula D, Cahill D G and Shim M, 2010 Lifetimes of optical phonons in graphene and graphite by time-resolved incoherent anti-stokes Raman scattering *Phys. Rev. B* **81** 165405.
- [64] Iglesias J M, Martín M J, Pascual E and Rengel R 2016 Hot carrier and hot phonon coupling during ultrafast relaxation of photoexcited electrons in

- graphene Appl. Phys. Lett. **108** 043105.
- [65] Golla D, A. Brasington A, Leroy J and Sandhu A 2017 Ultrafast relaxation of hot phonons in graphene-hBN heterostructures APL Materials **5** 056101.
- [66] Foster M S and Aleiner I L 2009 Slow imbalance relaxation and thermoelectric transport in graphene Phys. Rev. B **79** 085415.
- [67] Chatzakis I, Yan H, Song D and Berciaud S, and Heinz T F 2011 Temperature dependence of the anharmonic decay of optical phonons in carbon nanotubes and graphite Phys. Rev. B **83** 205411.
- [68] Klemens P G 1966 Anharmonic Decay of Optical Phonons Phys. Rev. **148** 845.
- [69] Zheng J-C, Zhang L, Kretinin A V, Morozov S V, Wang Yi Bo, Wang T, Li X, Ren F, Zhang J, Lu C-Yu, Chen J-C, Lu M, Wang H-Q, Geim A K and Novoselov K S 2016 High thermal conductivity of hexagonal boron nitride laminates 2D Materials **3** 011004.
- [70] Ryzhii V, Otsuji T, Ryzhii M, Ryabova N, Yurchenko S O, Mitin V and Shur M S 2013 Graphene terahertz uncooled bolometers J. Phys. D: Appl. Phys. **46** 065102.
- [71] Vasko F T and Ryzhii V 2008 Photoconductivity of intrinsic graphene Phys. Rev. B **77** 195433.
- [72] Satou A, Vasko F T and Ryzhii V 2008 Nonequilibrium carriers in intrinsic graphene under interband photoexcitation Phys. Rev. B **78** 115431.
- [73] Mahlmeister N H, Lawton L M, Luxmoore I J and Nash G R 2016 Modulation characteristics of graphene-based thermal emitters Appl. Phys. Express **9** 012105.
- [74] Rosencher E, Vinter B, Luc F, Thibaudeau L and Nagle J 1994 Emission and capture of electrons in multiquantum-well structures IEEE J. Quantum Electron. **30** 2875.
- [75] Aleshkin V Ya, Dubinov A A, Ryzhii M, Ryzhii V and Otsuji T 2015 Electron capture in van der Waals graphene-based heterostructures with WS<sub>2</sub> barrier layers J. Ohys. Soc. Japan **84** 094703.
- [76] Serov A Y, Ong Z-Y, Fischetti M V and Pop E 2014 Theoretical analysis of high-field transport in graphene on a substrate, Appl. Phys. **116** 034507.